Polypyrrole-Assisted Nitrogen Doping Strategy to Boost Vanadium Dioxide Performance for Wearable Nonpolarity Supercapacitor and Aqueous Zinc-Ion Battery

Jiabin Guo, Lei Li, Jie Luo, Wenbin Gong, Rui Pan, Bing He, Shuhong Xu, Meinan Liu, Yongjiang Wang, Baihe Zhang, Chunlei Wang,* Lei Wei, Qichong Zhang,* and Qingwen Li*

Fiber-shaped energy-storage devices with high energy and power density are crucial for powering wearable electronics. However, the improvement of their energy and power density is limited by the low mass loading of active materials and slow diffusion of ions, which further hinders the application as flexible energy-storage devices. Herein, a facile and cost-effective strategy is proposed to fabricate polypyrrole (PPy)-assisted nitrogen-doped vanadium dioxide/nitrogen-doped carbon (N–VO₂@NC) heterostructures by the pyrolyzation of vanadium oxide (VOₓ)/PPy supported on carbon nanotube fiber (CNTF). The carbonization of PPy nanowire not only forms nitrogen-doped carbon 3D conductive scaffold for enhancing ion transport pathways and mass loading of N–VO₂ but also provides source of nitrogen in situ doping into VOₓ to produce N–VO₂ for improving electronic conductivity and energy-storage capacity. Consequently, the well-designed N–VO₂@NC@CNTF electrode delivers impressive electrochemical performance and extraordinary mechanical flexibility both applied in all-solid-state fiber-shaped nonpolarity supercapacitors and aqueous zinc-ion batteries. Furthermore, the results of theoretical calculations discovered that the band gap of PPy-assisted N–VO₂ can be significantly reduced from 0.55 to 0.23 eV and thus its conductivity is greatly enhanced. This work sheds light on the construction of high-performance free-standing electrodes for next-generation wearable aqueous energy-storage devices.

1. Introduction

The booming reform of wearable electronics has put forward higher requirements for their energy supply system.[1–6] The ever-developing flexible energy-storage devices with bendable and foldable features are well matched, since can potentially be woven into the fabrics to solve the above challenges.[7–9] Recently, developed carbon-based fibers due to the merits of featuring light weight, superior conductivity, and omnidirectional flexibility are suitable as current collectors for realization of flexible energy-storage devices.[10–15] Therefore, the vast majority of spotlights mainly focused on exploring such fiber-shaped aqueous energy-storage devices including super-capacitors and aqueous ion batteries at present.[16–22] Unfortunately, the reported fiber-shaped electrodes are still inadequate for large-scale flexible energy storage, especially in practical applications. This may be ascribed to low specific capacitance, sluggish ionic diffusion, and poor electronic conductivity of the active material leading to suboptimal energy and power density, respectively.[23–26] Disadvantaged by these undesired outcomes, the development of flexible devices based on using carbon-based fibers as current collectors have been hampered for a long time.

Numerous methodologies are undertaken by material chemists or energy experts to address the mentioned above shortcomings.[27–34] Among them, doping heteroatoms into active materials is the one effective solution, which can change their electronic distribution in molecular structure thereby enhancing the electronic conductivity.[18,35–37] Another reported effective strategy is to load the active material onto a 3D scaffold, significantly increasing their load mass and specific surface area, which provide more

J. B. Guo, L. Li, R. Pan, S. H. Xu, C. L. Wang
School of Electronic Science & Engineering
Southeast University
Nanjing 210096, P. R. China
E-mail: wangchl@seu.edu.cn

J. Luo, M. N. Liu, Y. J. Wang, B. H. Zhang, Q. C. Zhang, Q. W. Li
Key Laboratory of Multifunctional Nanomaterials and Smart Systems
Suzhou Institute of Nano-Tech and Nano-Bionics
Chinese Academy of Sciences
Suzhou 215123, China
E-mail: zhangqc@ntu.edu.sg; qwli2007@sinano.ac.cn

W. B. Gong
School of Physics and Energy
Xuzhou University of Technology
Xuzhou 221018, China

B. He, L. Wei
School of Electrical and Electronic Engineering
Nanyang Technological University
Singapore 639798, Singapore

Y. J. Wang
Gusu Laboratory of Materials
Suzhou 215000, China

**ADVANCED
SCIENCE NEWS**
www.advancedsciencenews.com

**ADVANCED
ENERGY
MATERIALS**
www.advenergymat.de

ion storage sites and charge transmission paths to improve the capacitance and accelerate ionic diffusion, respectively.[38–40] For example, an effective doping strategy was reported by Yang et al. to prepare nitrogen-doped Co_3O_4 nanowires with improved the catalytic activity as an additive-free air-cathode for flexible zinc–air batteries.[41] Similarly, sulfur-doped MnO_2 nanosheets as a cathode toward Zn-ion batteries exhibited enhanced large discharge capacity, high-rate performance and long cycle life.[42] Moreover, porous hierarchical fabric as the conductive scaffold enables high areal capacitance loading in each electrode.[43–45] The utilization of highly conductive and flexible 3D electrode architecture also enables fast electron transport and rapid ion diffusion.[46] Although individually doping heteroatoms or using scaffolds are effective strategies, the promotion of electrochemical performances and mechanical properties of the fibrous electrodes is still limited, as well as requires a cumbersome manufacturing process. Accordingly, it would be expectant to simultaneously realize the aforementioned two improvements after one-step optimization in a simple experimental scheme. As a conductive polymer representative, polypyrrole (PPy) has been widely studied and can be synthesized into sundry nano-morphologies. When carbonized at high temperature in an inert gas, PPy can be converted into nitrogen-doped carbon and decomposed to release ammonia as N source.[47] Vanadium-based composites have attracted increasing attention owing to their diversiform valence states and manifold crystal structures.[48,49] Vanadium dioxide (VO_2) with affluent crystal structures as typical vanadium-based candidate has been applied in electrochemical energy storage devices as the active materials, but their sluggish ion diffusion and vulnerable chemical architecture dramatically limited rate performance and cycle stability.[50,51]

Based on the above considerations, as a proof-of-concept verification, we herein prepared nitrogen-doped vanadium dioxide/nitrogen-doped carbon (N–VO_2@NC) fibrous electrodes by electrochemical deposition of polypyrrole on carbon nanotube fiber (CNTF), solvothermal growth of vanadium oxide precursor, and heat treatment, used for all-solid-state fiber-shaped nonpolarity supercapacitors (FNSC) and aqueous zinc-ion batteries (FAZIB). Specifically, the nitrogen-doped carbon 3D conductive scaffold can be provided by using carbonized PPy loading VO_2 with a certain nano-morphology, while the N–VO_2 can be obtained by the pyrolytic of PPy to yield ammonia in situ supplying nitrogen for then doping. This clever design proves that can synchronously realize the doping nitrogen into VO_2 and the forming conductive 3D nitrogen-doped carbon scaffold through a simple annealing step. Subsequently, various electrochemical tests confirmed that the electrochemical performance of both the FNSC and FAZIB with great mechanical strength is significantly superior to that without nitrogen doping or nitrogen-doped carbon 3D conductive scaffolds, which adequately attested the meliority of introducing PPy. In addition, density functional theory (DFT) simulations were conducted to confirm above results that the N–VO_2 is more conducive to obtaining better electrochemical performance in comparison with those of the VO_2.

2. Results and Discussion

N–VO_2 nanosheets (NSs)@NC nanowires (NWs) heterostructure nanocomposites were synthesized through a facile three-step approach, as the introduced schematic shown in **Figure 1**a, including an electrochemical polymerization, solvothermal process, and a post-annealing procedure. A neat CNTF with a diameter of ≈100 μm (Figure S1, Supporting Information) was washed several times with ethanol and deionized water before using as current collector and substrate. As depicted in Figure 1b, pretty high aspect-ratio PPy NWs densely deposited on CNTF were observed after galvanostatic polymerization at 0.5 mA for 1 h. Owing to their large specific surface area, PPy NWs play the role of dual functions, not only could improve this nanocomposite electrical conductivity after carbonization treatment but also as a conductive scaffold to regulate the loading mass of the outer-layer active material. It is also important to mention that such dense PPy NWs would experience pyrolysis and release ammonia gas in situ, which can simultaneously induce the subsequently grown materials subjected to N elemental doping. Thus, the potential safety risk caused by the general use of additional dangerous gas, such as ammonia, could be drastically reduced. During the following solvothermal process, vanadium oxide NSs were successfully grown on as-synthesized PPy NWs@CNTF surface. As a result of the ammonia generated from PPy thermal decomposition, the N–VO_2 NSs wrapped NC structural skeletons were preserved on CNTF after annealing treatment in Ar at 600 °C for 2 h. The scanning electron microscope (SEM) images in Figure 1c,d shows a unique 3D core-shell structure fiber uniformly covered with dense NSs along the axis direction. Compared with the pristine CNTF, the N–VO2@NC@CNTF shows the significantly increased specific surface area and apparently reduced pore sizes (Figure S2, Supporting Information). As the transmission electron microscope (TEM) image in Figure 1e, the structural integrity is retained even after calcination and maintains the distinct features of high porosity and vast specific surface area. Furthermore, uniform distribution of C, N, V, and O elements in different regions were clearly found in the energy dispersive X-ray spectroscopy (EDX) patterns shown in Figure 1f. This satisfied observation further evidenced the formation of a typical N–VO_2@NC@CNTF core-shell structure. Therefore, a reasonable deduction could be made for the N source stemming from PPy pyrolysis. Moreover, it was significantly observed that the lattice fringes with an interlayer spacing of 3.21 Å in the high-resolution TEM (HRTEM) image of N–VO_2 NSs (Figure 1g), which is well consistent with the (011) crystallographic plane of monoclinic VO_2 (JCPDS card No. 43–1051). Additionally, it is also verified that the successful preparation of crystalline VO_2 NSs and the lattice structure of VO_2 was not affected by N doping. This special core-shell nanocomposite with high specific surface area affords significant improvements of ionic conductivity and experimental capacitance capacity, which are mainly ascribed to the dual functions of PPy NWs and will be detailly discussed in later sections.

The crystallization characterization of VO_2 based composites was further investigated using small-angle X-ray scattering (SAXS) technique, the representative 2D pattern and the calculated 1D curves were presented in **Figure 2**a,b. Initially, the typical ring patterns with uniform intensity distributions were obtained in Figure 2a, which indicated the isotropic and homogenous N–C NWs on CNTF surface. Besides, the diamond-like scattering pattern close to the central beam stop evidently
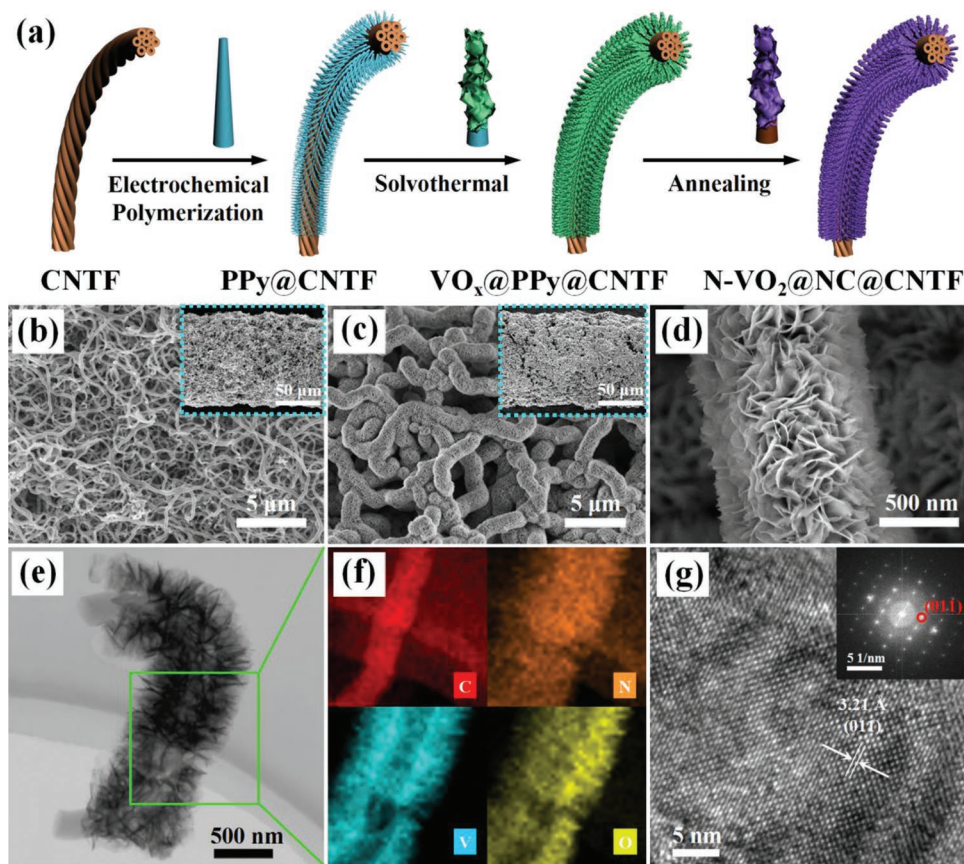
Figure 1. a) Schematic illustration of the preparation of N–VO$_2$@NC@CNTF. b) SEM image of the PPy NWs on CNTF. c,d) SEM images of N–VO$_2$@NC on CNTF at increasing magnifications. e) TEM image of N–VO$_2$@NC@CNTF and f) EDX elemental mappings of C, N, V, and O. g) HRTEM image of N–VO$_2$ NSs and the inset is the corresponding SAED pattern.

reveals the formation of regular oriented N–VO$_2$ nano lamellae on N–C NWs@CNTF composite. These observations are in good agreement with the SEM and TEM results presented in Figure 2b–f. The extracted 1D-SAXS intensity profiles of VO$_2$@NC@CNTF with/without N doping are depicted in Figure 2b to provide more quantitative and subtle information about VO$_2$. Several diffraction peaks of N–VO$_2$@NC@CNTF were observed and indicated by the red diamond marks at the scattering vector around 1.96, 2.59, and 2.93, which are corresponding to the (011), (−211), and (−212) crystal planes of monoclinic VO$_2$ (referred to the JCPDS PDF card with No. 43–1051), respectively. In addition, the black clubs represent the typical peaks of CNTF. In the case of VO$_2$@NC@CNTF, no remarkable changes occurred to the 1D SAXS curve, which strongly proved that the high lattice stability of VO$_2$ and no obvious lattice disorder phenomenon appeared even in the presence of N doping. In Figure 2c, the representative Raman spectrum of N–VO$_2$@NC@CNTF clearly shows several various vibration modes (V = O, V–O, and V^{4+} = O) at different shifts. As the electron paramagnetic resonance (EPR) spectrum shown in Figure 2d, another piece of evidence for N doping VO$_2$@NC@CNTF comes from an increased intensity signal at g = 2.003 resulting from the raising monoionized V + O vacancies, which were probably occupied by N after calcination treatment. In addition, the tiny vacancy defects V + O contribute to the improvement

of N–VO$_2$@NC@CNTF electrical conduction behavior.[52] X-ray photoelectron spectroscopy (XPS) measurement is a crucial mean to study substances' chemical composition and chemical state. The survey full XPS spectrum in Figure 2e confirms the presence of C, N, O, and V, while the C 1s, N 1s, V 2p, and O 1s spectra are demonstrated in Figures 2f,g,h, and 2i, respectively. The high-resolution N 1s spectrum only consists of two peaks at around 400 and 402 eV mainly corresponding to N–V in N–VO$_2$ and N–C in carbonized PPy scaffold, respectively. On the other hand, these detail spectra further prove the successful preparation of the N–VO$_2$@NC@CNTF electrodes.

N–VO$_2$@NC@CNTF composites are ideal energy-storage materials applied in novel FNSCs owing to its nature, 1D structure, good flexibility, brilliant conductivity, and large specific surface area. Therefore, the electrochemical performances of the as-prepared electrode materials were determined in 2 M LiCl aqueous electrolyte via a three-electrode configuration, whereas the utilization of N–VO$_2$@NC@CNTF, Ag/AgCl, and Pt wire as the working, reference, and counter electrodes, respectively. Moreover, N–VO$_2$@NC@CNTF could be employed as not only positive electrode but also negative electrode in FNSCs attributed to its nonpolar intrinsic nature. The electrochemical behaviors of the N–VO$_2$@NC@CNTF electrode at the positive potential range of 0–0.8 V versus Ag/AgCl are given in **Figure 3**a–f, where the identical measurements were repeated
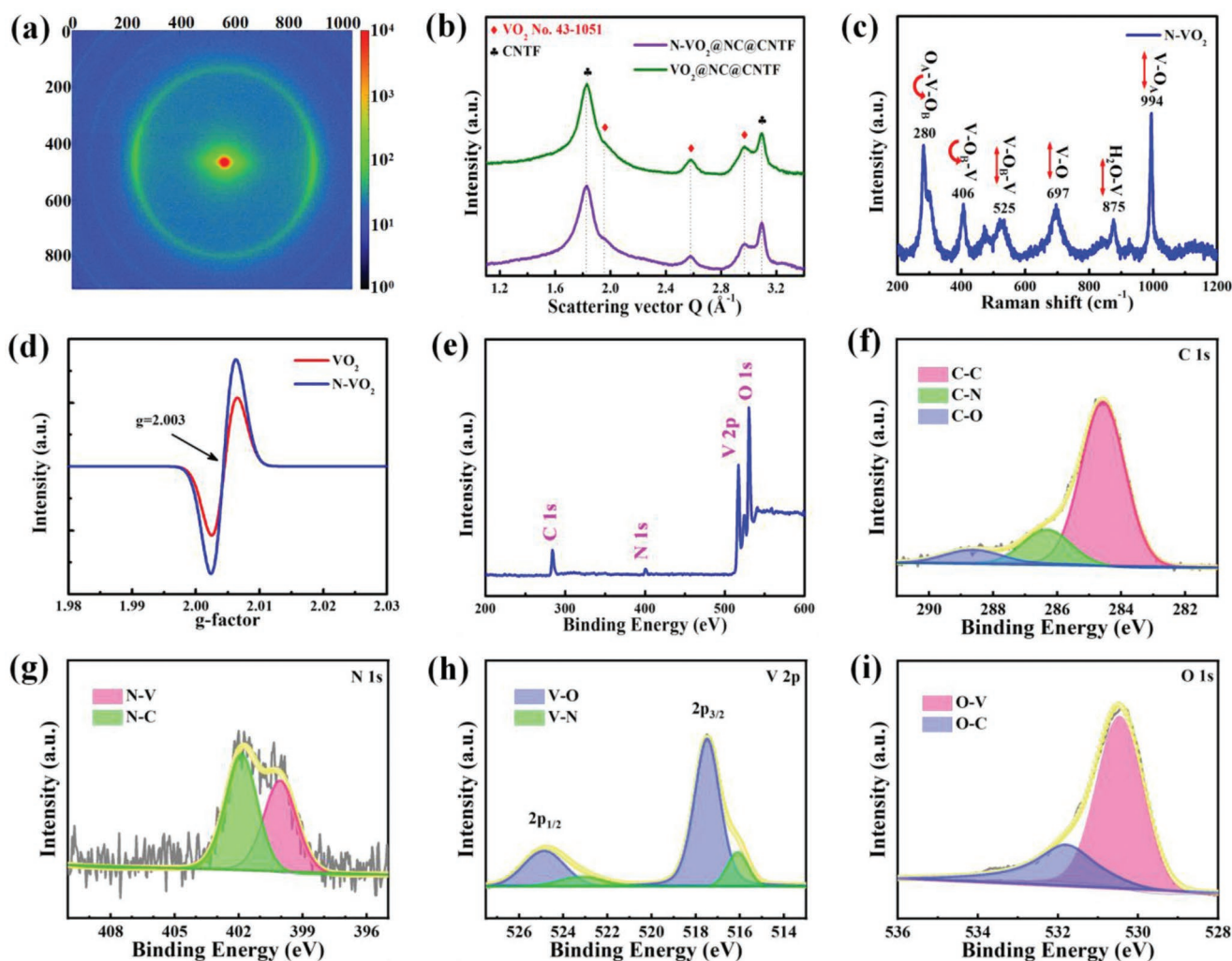
Figure 2. a) 2D SAXS pattern collected from N–VO$_2$@NC@CNTF. b) Extracted 1D-SAXS curves from (a). c) Raman spectrum, d) EPR spectra, and e) XPS spectra of N–VO$_2$@NC@CNTF. f–i) The high-resolution XPS spectra of C 1 s, N 1 s, V 2p, and O 1 s.

but at more negative potential range of −1.2 to 0 V are shown in Figure 3g–l. In detail, a series of experiments were designed and conducted to evaluate the effects of NC NWs conductive scaffold and N doping on those selected electrodes electrochemical performance (Figures S3–S6, Supporting Information). As the CV responses shown in Figure 3a,g, among all the selected fiber electrodes, N–VO$_2$@NC@CNTF electrode presented superior electrochemical behaviors evidenced by the highest current value. Compared with the negligible electrochemical performance of pristine CNTF and NC@CNTF, on the one hand, VO$_2$ extraordinarily enhances the capacitance due to the pretty big specific surface area and highly crystalline orientation. On the other hand, NC NWs as a conductive scaffold extremely improve the active material VO$_2$ loading mass as well as stimulate the N elemental doping of VO$_2$, which would be beneficial for ionic migration. In Figure 3b,h, the N–VO$_2$@NC@CNTF electrodes were further investigated over a range of scan rates of 5–200 mV s^{-1} at two different potential windows. All CV curves behaved quasi-rectangular shapes without any typical redox peak pairs even at a higher sweep rate, indicating

that the ideal reversible capacitive performance and desirable rapid charge/discharge process of N–VO$_2$@NC@CNTF electrodes. Additionally, the current response composition could be divided into capacitive contribution and ionic diffusion contribution:[53,54]

$$i = k_1 v + k_2 v^{1/2} \tag{1}$$

where k_1 and k_2 represent the proportional coefficients of capacitance and diffusion contribution, and v is the scan rate. Each proportion can be determined according to this equation. As displayed in Figure 3c,i, the capacitance contribution accounts for about 96.19% at 100 mV s^{-1} at positive potential range and 95.33% at 200 mV s^{-1} at negative potential range, respectively. Furthermore, it can be clearly found that the capacitance contribution ratio shows a gradual increase trend as the scan rate raises (Figure 3d,j), indicating again that the dominant capacitance contribution mainly ascribed to the synergic effect of NC NWs and the high specific surface area of N–VO$_2$. Rate performance is generally considered as a key index to evaluate the
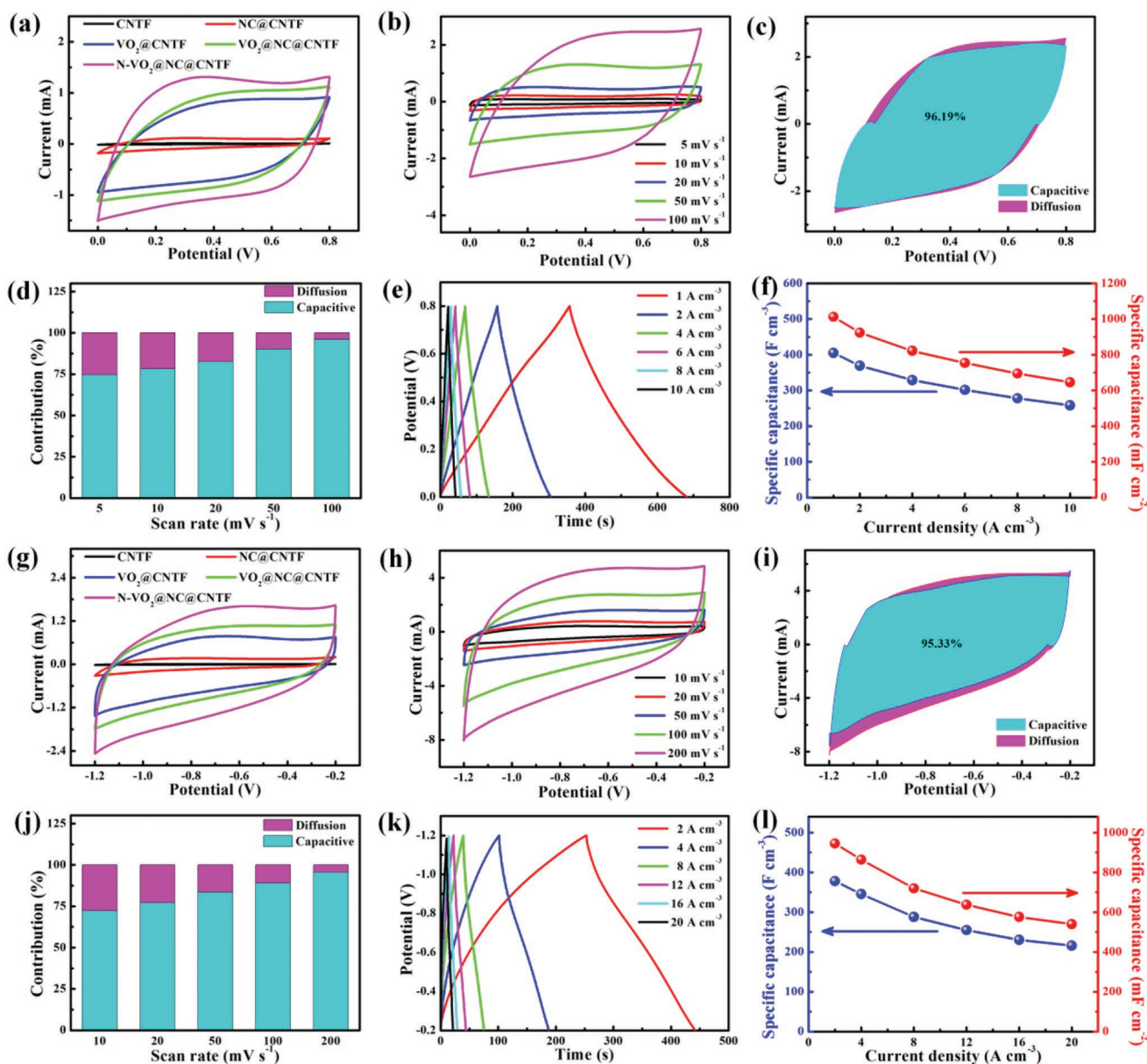
**ADVANCED
SCIENCE NEWS**
www.advancedsciencenews.com

**ADVANCED
ENERGY
MATERIALS**
www.advenergymat.de

Figure 3. Electrochemical performance of N–VO$_2$@NC@CNTF electrode in a 2 M LiCl aqueous electrolyte at the potential ranges of 0–0.8 V or –1.2 to –0.2 V (vs Ag/AgCl). a,g) CVs of selected electrodes at ν = 50, 100 mV s^{-1}, respectively; b,h) CVs recorded at various scan rates; c,i) the capacitive contribution recorded at specified 100, 200 mV s^{-1}, respectively; d,j) the capacitive contributions at various scan rates; e,k) GCD curves at various current densities; f,l) areal and volumetric specific capacitances computed from the corresponding discharge curves in (e) and (k), respectively.

SCs electrodes for potential practical applications, which corresponds to the symmetry degree of the galvanostatic charge/discharge (GCD) curves. The representative GCD curves of N–VO$_2$@NC@CNTF electrodes at 1–20 A cm^{-3} are recorded in Figure 3e,k, these nearly perfect symmetrical triangle shapes again demonstrated that this robust material owns excellent capacitance. The areal and volumetric specific capacitances were calculated from the corresponding GCD curves concluded in Figure 3f,l. The N–VO$_2$@NC@CNTF electrode exposes a brilliant specific capacitance, as shown in Figure 3f, as high as 405 F cm^{-3} (1012.5 mF cm^{-2}) and 258.19 F cm^{-3} (645.47 mF cm^{-2}) at 1, 10 A cm^{-3}, respectively. In addition, only a slight specific

capacitance loss was observed and presented in Figure 3l, such outstanding outcomes derive from their excellent conductivity and large physical specific surface area that can boost the active materials deposition and extraction.

In order to further explore the practicability of nonpolar N–VO$_2$@NC@CNTF electrode served as supercapacitor, two same N–VO$_2$@NC@CNTF electrodes coating with LiCl/polyvinyl alcohol (LiCl–PVA) gel electrolyte were wound to construct a quasi-solid-state flexible FNSC, as shown in the schematic diagram in **Figure 4**a. The working voltage of the FNSC is forecast to reach 2.0 V due to the fact that the positive potential range of the N–VO$_2$@NC@CNTF electrode is from 0 to 0.8 V, while the
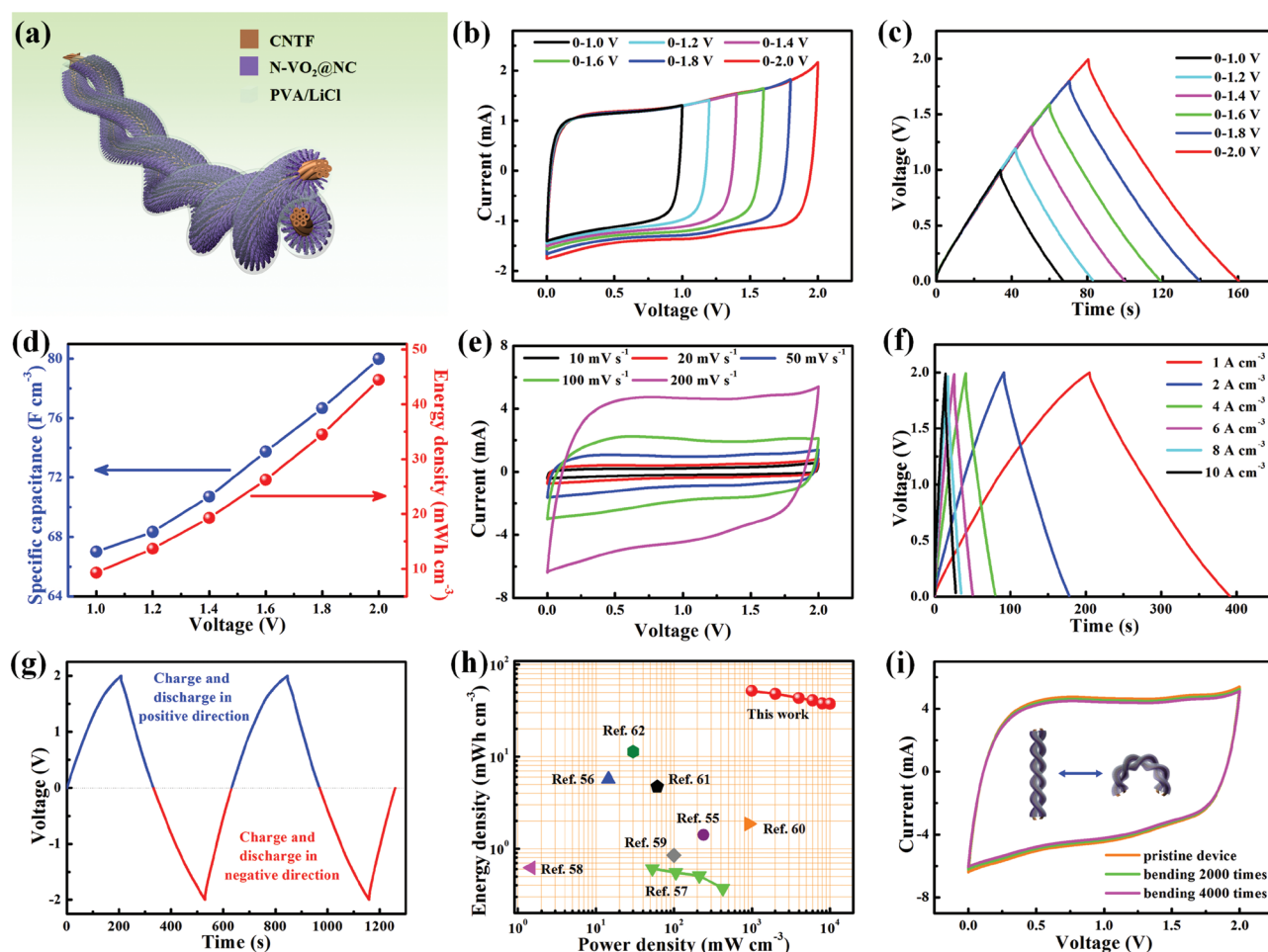
Figure 4. Electrochemical properties of the quasi-solid-state nonpolar FNSC wound by two same N–VO$_2$@NC@CNTF electrodes coating with LiCl/PVA gel electrolyte. a) Schematic diagram of the FNSC. b) CV curves of the FNSC at the constant scan rate of 100 mV s^{-1} within different working voltages. c) GCD curves of the FNSC acquired with the immobile current density of 2 A cm^{-3} in various voltages from 1.0 to 2.0 V. d) Volumetric specific capacitances and energy densities calculated from the corresponding discharge curves. e) CV curves of the FNSC with 2.0 V working voltage at the changing scan rates from 10 to 200 mV s^{-1}. f) GCD curves with sliding current densities from 1 to 10 A cm^{-3} with 2.0 V working voltage. g) GCD curves in both positive and negative directions. h) The Ragone plot of volumetric energy densities versus power densities of the FNSC in this work and previously published high performance devices. i) CV curves of the FNSC with changed bending cycles under the scan rate of 200 mV s^{-1}.

negative potential range of the N–VO$_2$@NC@CNTF electrode is from −1.2 to 0 V. For verification, CV (Figure 4b) at the constant scan rate of 100 mV s^{-1} and GCD (Figure 4c) acquired with the immobile current density of 2 A cm^{-3} of the FNSC in various voltages from 1.0 to 2.0 V have been performed. As expected, with the working voltage rising from 1.0 to 2.0 V, the shapes of CV and GCD curves maintain quasi-rectangle and triangle without deformation respectively, supporting the feasibility of working voltage of 2.0 V of the FNSC. Volumetric specific capacitances and energy densities of increasing working voltages calculated from the corresponding discharge curves at 2 A cm^{-3} are also displayed in Figure 4d, in which the volumetric specific capacitance of FNSC is greatly improved from 67 to 80 F cm^{-3} while the energy density is superbly promoted from 9.31 to 44.44 mWh cm^{-3}, as a result of reaching such a high working voltage (2.0 V) from 1.0 V. Figures 4e and 4f provide CV curves at varied scan rates and GCD curves at various current densities

of the FNSC within the working voltage of 2.0 V, respectively. These curves of quasi-rectangles and isosceles triangle once more demonstrate the outstanding capacitive behavior of the FNSC. The volumetric and areal specific capacitances of the FNSC calculated according to the corresponding discharge curve in Figure S7, Supporting Information, shows that the FNSC has an excellent specific capacitance of 93.25 F cm^{-3} (233.125 mF cm^{-2}) at a current density of 1 A cm^{-3}, and still retains 67.5 F cm^{-3} (168.75 mF cm^{-2}) at ten times the current density, suggesting remarkable rate performance. In addition, the FNSC possesses extraordinary cycle performance of 90.16% capacitance retention after 5000 cycles of charge and discharge (Figure S8, Supporting Information). The Nyquist plot of the FNSC illustrated in Figure S9, Supporting Information, is also gained with frequencies from 10^{-2} to 10^5 Hz, where the equivalent series resistance of 13.4 Ω and the charge transfer resistance (R_{ct}) of 38.3 Ω further indicate the excellent conductivity

of the FNSC. The characteristics of nonpolarity of the FNSC are studied in Figure 4g by charging and discharging the identical device between −2 and 2 V. The blue curve shows the charge and discharge in the positive direction, while the red curve is equivalent to the charge and discharge in the negative direction. Even when charging and discharging back and forth between −2 and 2 V, the shape of GCD of the FNSC remains same triangular, which sufficiently proves the nonpolarity. Furthermore, flexibility for wearable devices is a vital index that cannot be ignored. As shown in Figure 4h, the device delivered a high volumetric energy density of 51.8 mW h cm^{-3} at a power density of 1000 mW cm^{-3}. As the power density increases, the energy density decreases to some extent, but can still retain 37.5 mW h cm^{-3} at a high power density of 10 000 mW cm^{-3}. This energy density value is also higher than that of recently reported fiber-based devices, including MoS$_2$/rGO/MWCNT fiber,[55] PANI/rGO fiber,[56] graphene NSs@TiN/C fiber//graphene NSs@Fe$_2$N C fiber,[57] Co$_3$O$_4$/Ni wire//rGO/C fiber,[58]

CuO@AuPd@MnO$_2$/Cu wire//Fe$_2$O$_3$@C/C fiber wire,[59] CuO@LDH NWAs/Cu//Cu/AC,[60] Ni$_{0.25}$Mn$_{0.75}$O@C//AC,[61] MnO$_2$/PEDOT: PSS/CNTF//ordered microporous C/CNTF,[62] and so on. As revealed in Figure 4i and Figure S10, Supporting Information, CV curves with negligible change and the capacitance retention rate of 97.08% after 4000 bending cycles prove the prominent flexibility of FNSC as wearable electronics. The series and parallel connections of devices are a common and valid way to extend the working voltage and output current. In the case of Figure S11, Supporting Information, two FNSCs obtain approximately twice the output voltage and capacitance of a single one when connected in series and parallel, respectively.

Besides the application in supercapacitors, VO$_2$ is also a kind of promising cathode material for AZIBs. Thus, electrochemical investigations of the quasi-solid-state FAZIB wound by N-VO$_2$@NC@CNTF cathode and Zn@CNTF anode (Figure S12, Supporting Information) coating with ZnSO$_4$/CMC

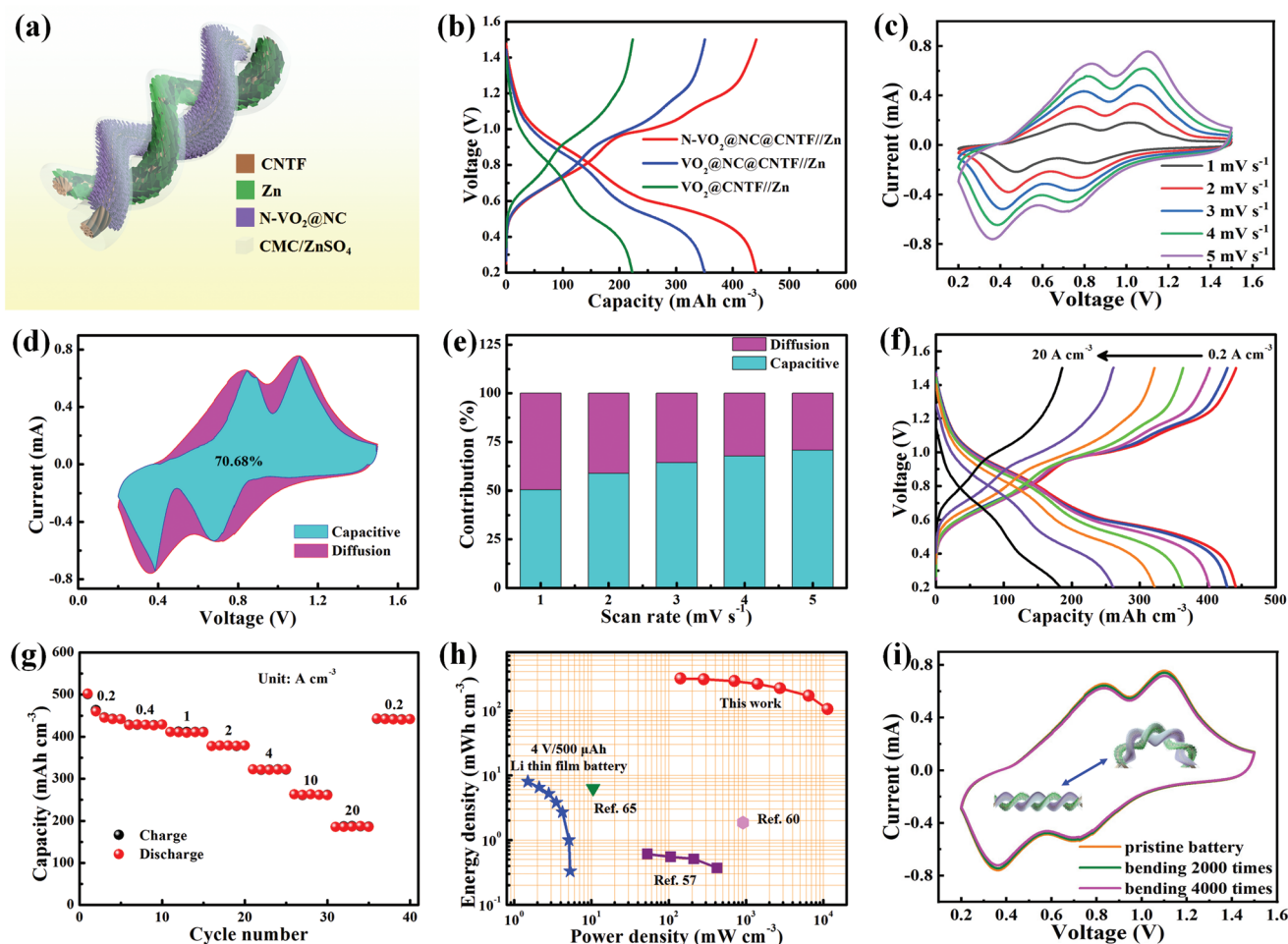**Figure 5.** Electrochemical performance of the quasi-solid-state FAZIB wound by N–VO$_2$@NC@CNTF and Zn@CNTF electrodes coating with ZnSO$_4$/CMC gel electrolyte. a) Schematic diagram of the FAZIB. b) Comparison of GCD curves of the VO$_2$@CNTF//Zn@CNTF, VO$_2$@NC@CNTF// Zn@CNTF, and N–VO$_2$@NC@CNTF//Zn@CNTF batteries at the current density of 0.2 A cm^{-3}. c) CV curves of the FAZIB at variational scan rates from 1 to 5 mV s^{-1}. d) The capacitive contribution of the FAZIB at 5 mV s^{-1}. e) The capacitive contributions of the FAZIB at varying scan rates. f) GCD curves of the FAZIB at different current densities between 0.2 and 20 A cm^{-3}. g) Rate capability of the FAZIB. h) The Ragone plot of volumetric energy densities versus power densities of the FAZIB in this work and previously published high performance devices. i) CV curves of the FAZIB with changed bending cycles under the scan rate of 5 mV s^{-1}.

**ADVANCED
SCIENCE NEWS**

www.advancedsciencenews.com

**ADVANCED
ENERGY
MATERIALS**

www.advenergymat.de

gel electrolyte have been implemented, which is exhibited by the schematic diagram in **Figure 5**a. Similarly, the superiority of NC NWs scaffold and N doping are again certified through the CV curves of Figure 5b, where $VO_2@NC@CNTF//Zn@CNTF$ compared to $VO_2@CNTF//Zn@CNTF$ and $N-VO_2@NC@CNTF//Zn@CNTF$ compared to $VO_2@NC@CNTF//Zn@CNTF$ both have a significantly increased specific capacity with the same assembling means. Moreover, GCD curves of the FAZIB at variational scan rates are presented in Figure 5c. It is apparently observed that the curves have two pairs of peaks of oxidation and reduction, which is derived from the multistep intercalation/deintercalation mechanism for Zn^{2+}. The electrochemical dynamic process is generally analyzed by the power law relationship between the scanning rate v and the peak current i in CV curves:[63,64]

$$i = av^b \qquad (2)$$

where a and b are constant parameters, b equal to 0.5 represents the diffusion control process and equal to 1 represents the capacitance control process. For the FAZIB, the b values corresponding to the four CV peaks are 0.829, 0.887, 0.814, and 0.782 respectively (Figure S13, Supporting Information), which means that the charge storage is mainly a fast and reversible surface process. As another evidence, Figure 5d,e gives the capacitive contributions of the FAZIB at varying scan rates, where the capacitance accounts for about 70.68% at 5 mV s^{-1} of the FAZIB and as the scan rates increase, the contribution rate of capacitance shows a gradual upward trend of the complete capacity. As Figure 5f supplies, GCD curves possess obvious charging and discharging plateaus of the FAZIB at all different current densities from 0.2 to 20 A cm^{-3}. Combined with the rate performance in Figure 5g, the FAZIB obtained an outstanding specific capacity of 441.383 mAh cm^{-3} at the current density of 0.2 A cm^{-3} and can still maintain 187.368 mAh cm^{-3} at 100 times of current density, indicating the brilliant rate capability due to the promotion of conductivity from the NC NWs scaffold. Besides, the cyclic stability of the FAZIB was also tested as demonstrated in Figure S14, Supporting Information, from which it can be seen that the FAZIB has a significant capacity retention rate of 85.61% and almost 100% wonderful coulombic efficiency after 500 charge and discharge cycles under high current, implying the good stability and once again confirming the benefits of NC NWs scaffold. The Nyquist plot of the FAZIB illustrated in Figure S15, Supporting Information, is also gained with frequencies from 10^{-2} to 10^5 Hz, where the equivalent series resistance of 10.7 Ω and small semicircles representing low charge transfer resistance calculated as 45.4 Ω again verifying the advantages of NC NWs scaffold. Figure 5h compares the volumetric performance of our FAZIB to those of reported available energy-storage devices. Our device delivered a high volumetric energy density of 313.13 mW h cm^{-3} at a power density of 142 mW cm^{-3}. As the power density increases, the energy density decreases to some extent, but can still retain 105.26 mW h cm^{-3} at a high power density of 11 356 mW cm^{-3}. This energy density value is also higher than that of recently reported fiber-based devices, including the 4 V/500 mAh thin-film lithium battery, graphene NSs@TiN/C fiber//graphene NSs@Fe$_2$N C fiber,[57] CuO@LDH NWAs/Cu//Cu/AC,[60]

SWNTs microfiber interposed N-doped reduced graphene oxide sheets, and so on.[65] Moreover, flexibility of the FAZIB is also revealed in Figure 5i and Figure S15, Supporting Information, CV curves with negligible change and the capacitance retention rate of 96.70% after 4000 bending cycles prove the prominent flexibility of FAZIB as wearable electronics. Similar to supercapacitors, two FAZIBs can obtain approximately twice the output voltage and capacitance of a single one in series and parallel connections, respectively (Figure S17, Supporting Information). Finally, the FAZIB was integrated with a commercial solar cell to construct a self-power device and its light-charge and galvanostatic discharge performances are provided in Figure S18, Supporting Information, suggesting the FAZIB a promising candidate for next-generation wearable self-powered devices.

The operating mechanism of batteries is closely concerned by researchers, so the ion intercalation and deintercalation mechanism of the FAZIB has been deeply studied, as the schematic diagram exhibited in **Figure 6**a. Figure 6b offers the first cycle of GCD curve of the FAZIB, where the points of various colors correspond to the SAXS curves with the same colors in Figure 6c. Obviously, during the pristine FAZIB was discharged to 0.2 V, the diffraction peaks of $Zn_4(OH)_6SO_4·4H_2O$ (orange region, JCPDS card No. 44–0673) and $Zn_4(OH)_6SO_4$ (pink region, JCPDS card No. 35–0910) are generated, while as the FAZIB was subsequently charged to 1.4 V, these peaks gradually disappeared, which is the indirect evidence that H$^+$ is involved in intercalation and deintercalation process. Additionally, the peak at the scattering vector Q of ≈2.93 with a shift during discharging and a recovery after charging suggests that Zn^{2+} ions intercalation during discharge and deintercalation during charging are first enlarged and then restored the spacing of VO_2 crystal planes. High-resolution XPS spectra of V 2p and Zn 2p at different discharged and charged states are also displayed by Figure 6d,e. During the discharge process, V^{4+} gradually decreased while V^{3+} increased stage by stage, which is consistent with the mechanism of ion intercalation and deintercalation. In addition, the mass of Zn in the electrode added in discharge step and reduced in charge procedure is a direct fact supporting the intercalation and deintercalation of Zn^{2+} in the operating process of the FAZIB. Another rationale is afforded by Raman spectra of the $N-VO_2@NC@CNTF$ electrode at various discharged–charged states (Figure 6f), in which the appearance and disappearance of Zn–O and new V–O vibration modes in discharge and charge courses still suggesting the intercalation and deintercalation of Zn^{2+}. Furthermore, TEM images and corresponding EDX elemental mapping images of the $N-VO_2@NC@CNTF$ electrode at different discharged and charged states are set out in Figure 6g–i. Besides the elements N, V, and O arisen from $N-VO_2$ NSs, the increase and decrease of element Zn and S during the discharge and charge again certify the Zn^{2+} and H$^+$ dual ion insertion mechanism.

To demonstrate the relation between the crystal structures and the performances of VO_2 and $N-VO_2$, DFT simulations were performed in this study. Based on the experimental observations, the $N-VO_2$ structure was structured by randomly replacing O atom of VO_2 with N atom, as shown in **Figure 7**a,b. From the calculated density of states (DOS) illustrated in Figure 7c, it is easy to find that the doping of N can improve the

**ADVANCED
SCIENCE NEWS**

www.advancedsciencenews.com

**ADVANCED
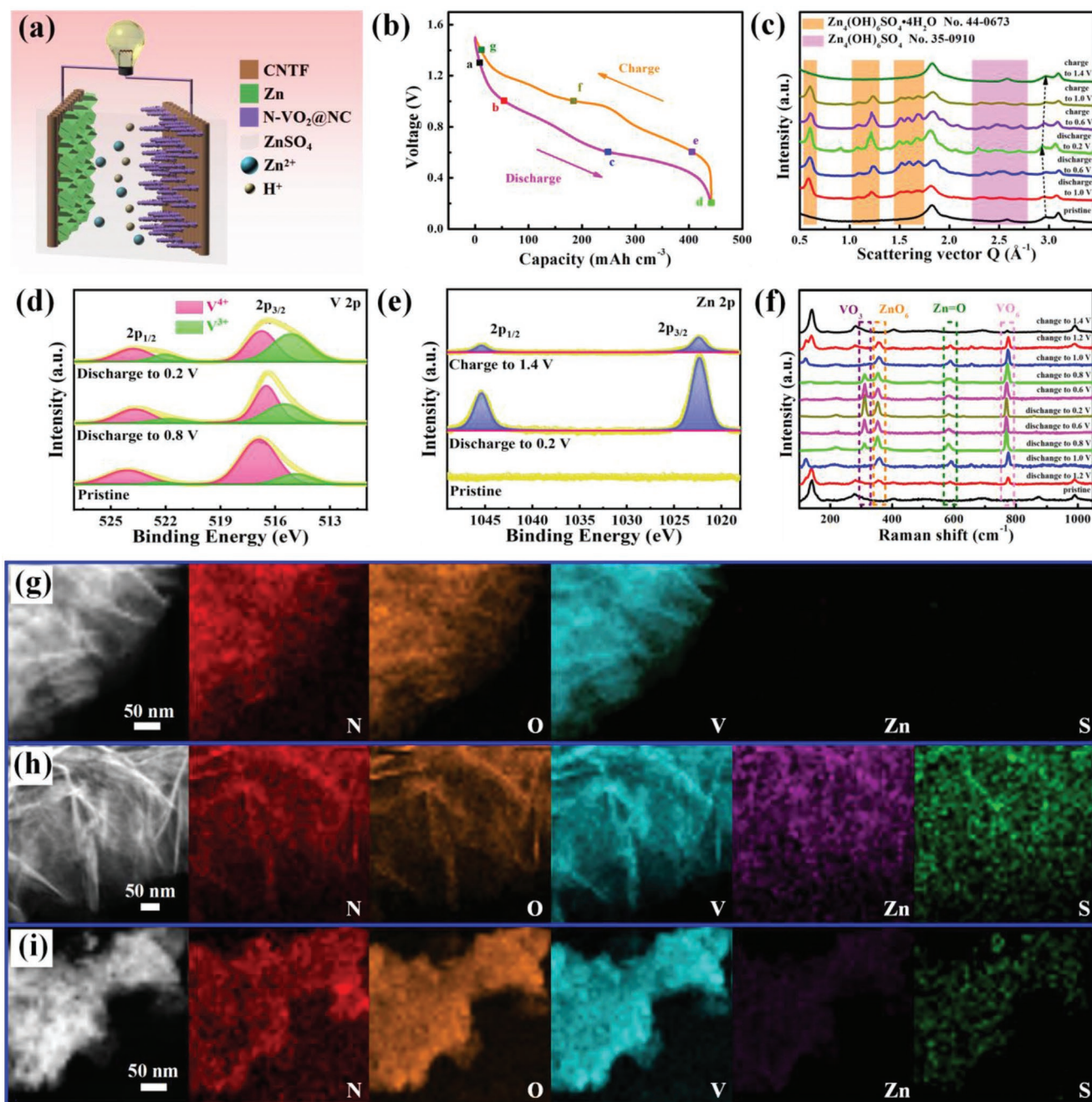ENERGY
MATERIALS**

www.advenergymat.de

Figure 6. a) Schematic diagram of the intercalation reaction mechanism of the FAZIB. b) A cycle of typical GCD curve of the FAZIB. c) XRD spectra of the N–VO$_2$@NC@CNTF electrode at various discharged/charged states. High-resolution XPS spectra of d) V 2p and e) Zn 2p at different discharged/charged states. f) Raman spectra of the N–VO$_2$@NC@CNTF electrode at various discharged/charged states. TEM images and corresponding EDX elemental mapping images of the N–VO$_2$@NC@CNTF electrode of g) pristine, h) discharged to 0.2 V, and i) subsequently charged to 1.4 V.

electronic properties of VO$_2$, since the band gap reduces from 0.55 to 0.23 eV. Meanwhile, the existence of N atom in VO$_2$ also improves the binding strength of Li, as shown in Figure 7d–f. The binding energy of Li on the VO$_2$ (110) surface, which is the most stable one, is 3.18 eV. The strength increases to 3.47 eV when the O atom was substituted with N atom. Furthermore, as represented in Figure 7g–i, the Zn diffusion in the vicinity of N atom of N–VO$_2$ is about 0.04 eV, which is only about 28.5% of that of VO$_2$ (0.14 eV). These results illustrated that the doping

of N in N–VO$_2$ is beneficial to achieving a better performance than the pristine VO$_2$ structure.

3. Conclusion

In summary, we have demonstrated a simple approach using nitrogen-containing polymers to load active materials followed by carbonization to simultaneously realize nitrogen doping
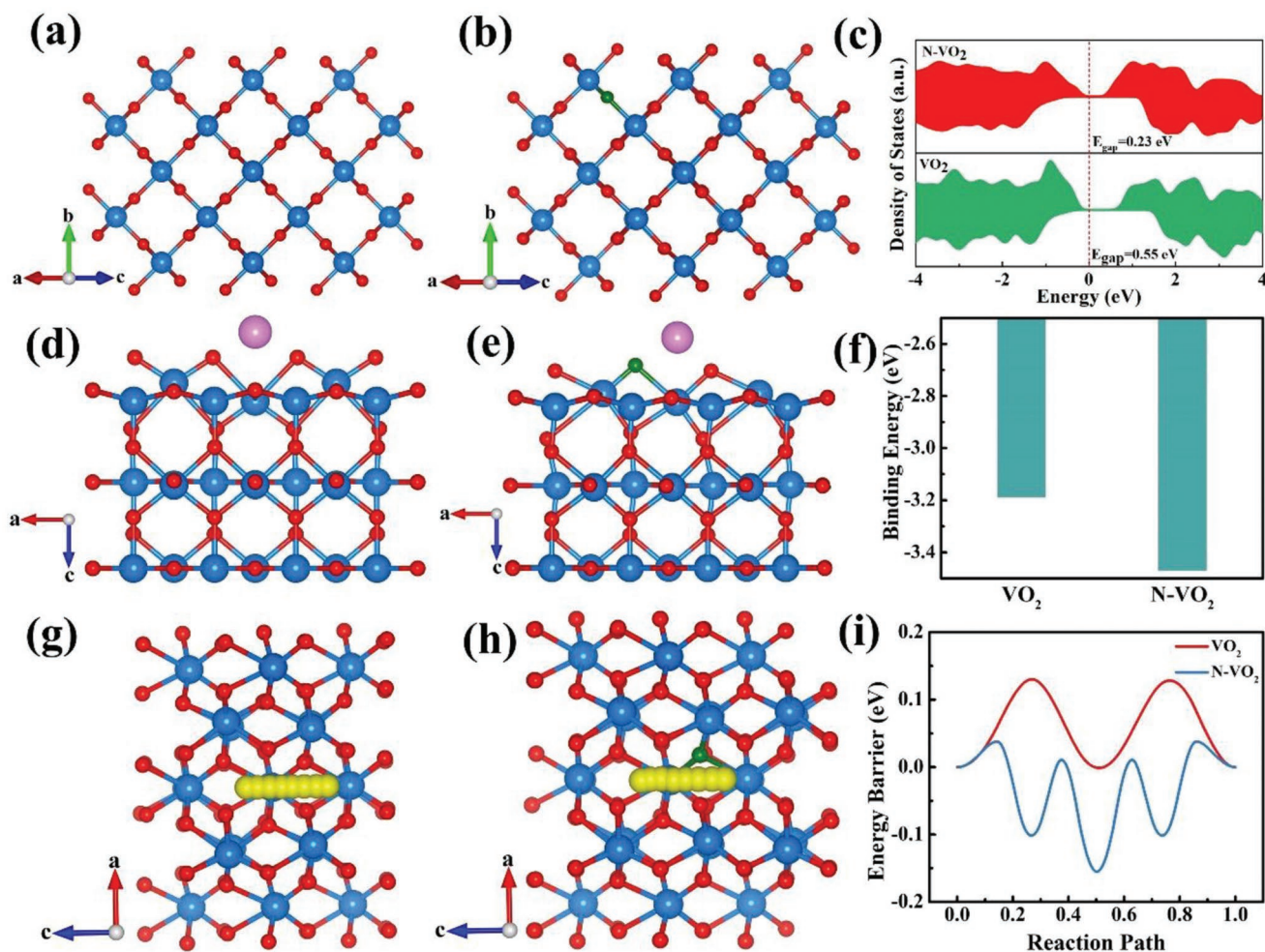
Figure 7. Theoretical investigations on performances of VO_2 and $N–VO_2$. a) Optimized structures of VO_2 and b) $N–VO_2$. c) The corresponding density of states of VO_2 and $N–VO_2$. Adsorption structures of Li atom on the (110) surfaces of d) VO_2 and e) $N–VO_2$, as well as f) their binding strengths. Diffusion paths of Zn^{2+} in g) VO_2 and h) $N–VO_2$. i) The corresponding diffusion energy barrier curves.

and provide nitrogen-doped carbon 3D conductive scaffolds, which provides a universal key for enhancing the performance of fibrous electrodes. To prove this concept, the well-designed N–VO₂@NC@CNTF fibrous electrode has been successfully developed via above-described strategy. Due to the synergistic effect of doping and the use of 3D conductive scaffold, the resulting fibrous electrode exposes a brilliant specific capacitance of 405 F cm⁻³ (1012.5 mF cm⁻²) with the current density of 1 A cm⁻³ in the positive potential range and an excellent specific capacitance of 378 F cm⁻³ (945 mF cm⁻²) at the current density of 2 A cm⁻³ in the negative potential range. Therefore, a FNSC is obtained by winding two identical N–VO₂@NC@CNTF electrodes coating LiCl/PVA gel electrolyte with excellent performance of capacitance of 93.25 F cm⁻³ (233.125 mF cm⁻²) and energy density of 44.44 mWh cm⁻³, and outstanding flexibility to maintain 97.08% of initial capacitance after 4000 bending cycles. Apart from assembling FNSC, these N–VO₂@NC@CNTF and Zn@CNTF electrodes coated with ZnSO₄/CMC gel electrolyte were wound to assemble a FAZIB, which possessed remarkable capacity of 441.383 mAh cm⁻³ at the current density of 0.2 A cm⁻³ and prominent energy density of 313.13 mWh

cm⁻³, with wonderful flexibility of 96.70% capacitance retention after 4000 bending cycles. Undoubtedly, these results prove that in suit generated N–VO₂ loading N-doped carbon 3D conductive scaffolds fibrous electrodes by one-step carbonization of PPy might open new avenues for the design and development of wearable aqueous energy-storage devices with excellent electrochemical performance and remarkable mechanical flexibility.

4. Experimental Section

Preparation of the PPy NWs@CNTF: PPy NWs were synthesized on CNTF via an electrochemical polymerization method. Typically, 7.703 g Na₂HPO₄·12H₂O, 3.120 g NaH₂PO₄·2H₂O, 1.942 g pyridine *p*-toluenesulfonate, and 0.694 mL pyrrole were added together into 100 mL deionized water under vigorous stirring for 30 min. A three-electrode setup was applied for PPy NWs growth in the mixed solution, in which the fresh CNTF was used as the working electrode, saturated calomel electrode and Pt wire were used as reference electrode and counter electrode, respectively. Subsequently, the polymerization reaction was triggered by applying a current of 0.5 mA. After 1 h, PPy NWs evenly coated CNTF (PPy NWs@CNTF) was obtained and rinsed with plenty of deionized water followed by drying it at 60 °C overnight.

Preparation of the N–VO2@NC@CNTF: The N–VO$_2$@NC@CNTF nanocomposites were synthesized through a solvothermal process followed by an annealing treatment. Typically, 0.3 mL vanadium oxytriisopropoxide was added into 45 mL isopropanol alcohol under vigorous stirring for 3 min. Then the mixed solution and PPy NWs@CNTF were transferred into a 50 mL Teflon-lined autoclave and heated for 10 h at 200 °C. After spontaneous cooling to room temperature, the prepared vanadium oxide precursors on PPy NWs@CNTF were washed with ethanol for several times and dried at 60 °C overnight. At last, the N–VO$_2$@NC@CNTF fiber electrodes were successfully gained after annealing treatment in Ar atmosphere with 200 sccm at 600 °C for 2 h. For the sake of comparison, VO$_2$@CNTF and VO$_2$@NC@CNTF were prepared as well, similar to N–VO$_2$@NC@CNTF procedures but with several fine modifications. Detailly, deleted the step of PPy NWs polymerized on CNTF to prepare VO$_2$@CNTF, and added carbonization treatment before the solvothermal process to obtain VO$_2$@NC@CNTF.

Assembling of the FNSCs: The FNSC was assembled by twining two N–VO$_2$@NC@CNTF electrodes decorated with LiCl/PVA gel electrolyte. In detail, 4.3 g LiCl and 10 g PVA were added into 100 mL deionized water under vigorous stirring for 2 h at 95 °C until it changed to colorless. Subsequently, two identical N–VO2@NC@CNTF electrodes were separately immersed into LiCl/PVA gel electrolyte for 10 min and then dried at 60 °C for 30 min. Finally, the two as-prepared electrodes were twined together after repeating immersion treatment one more time and dried overnight.

FAZIB Assembling: Zn electrodes were prepared on CNTF via an electrochemical method. Typically, 5 g ZnSO$_4$·7H$_2$O, 5 g Na$_2$SO$_4$, and 0.8 g H$_3$BO$_3$ were added together into 40 mL deionized water under vigorous stirring for 45 min. The electrochemical deposition of Zn on CNTF was performed in the mixed solution in a three-electrode configuration with a constant current density of −0.05 A cm$^{−2}$ for 20 min, where using a fresh CNTF, Ag/AgCl electrode, and Pt wire as the working electrode, reference electrode, and counter electrode, respectively. The FAZIB was assembled by twining N–VO$_2$@NC@CNTF cathode and Zn@CNTF anode decorated with CMC/ZnSO$_4$ gel electrolyte. Typically, 10 g ZnSO$_4$ and 6 g CMC were added into 100 mL deionized water under vigorous stirring for 2 h at 85 °C. Analogous assembling procedures of FNSC were carried out again by twisting CMC/ZnSO$_4$ gel decorated N–VO$_2$@NC@CNTF and Zn@CNTF electrodes to form FAZIB device.

Supporting Information

Supporting Information is available from the Wiley Online Library or from the author.

Acknowledgements

Conflict of Interest

The authors declare no conflict of interest.

Data Availability Statement

The data that support the findings of this study are available from the corresponding author upon reasonable request.

[1] Z. N. Li, S. Gadipelli, H. C. Li, C. A. Howard, D. J. L. Brett, P. R. Shearing, Z. X. Guo, I. P. Parkin, F. Li, *Nat. Energy* **2020**, *5*, 160.

[2] Y. Q. Yang, Y. Tang, G. Z. Fang, L. T. Shan, J. S. Guo, W. Y. Zhang, C. Wang, L. B. Wang, J. Zhou, S. Q. Liang, *Energy Environ. Sci.* **2018**, *11*, 3157.

[3] C. W. Li, L. Li, B. He, Y. Ling, J. Pu, L. Wei, L. T. Sun, Q. C. Zhang, Y. G. Yao, *Mater. Sci. Eng., R* **2022**, *148*, 100671.

[4] L. B. Liu, Y. Yu, C. Yan, K. Li, Z. J. Zheng, *Nat. Commun.* **2015**, *6*, 7260.

[5] D. L. Chao, C. R. Zhu, M. Song, P. Liang, X. Zhang, N. H. Tiep, H. F. Zhao, J. Wang, R. M. Wang, H. Zhang, H. J. Fan, *Adv. Mater.* **2018**, *30*, 1803181.

[6] X. Pu, W. X. Song, M. M. Liu, C. W. Sun, C. H. Du, C. Y. Jiang, X. Huang, D. C. Zou, W. G. Hu, Z. L. Wang, *Adv. Energy Mater.* **2016**, *6*, 1601048.

[7] L. Wang, X. Fu, J. He, X. Shi, T. Chen, P. Chen, B. Wang, H. Peng, *Adv. Mater.* **2020**, *32*, 1901971.

[8] X. Wu, X. Zhu, H. Tao, G. Wu, J. Xu, N. Bao, *Angew. Chem., Int. Ed.* **2021**, *60*, 21295

[9] L. Li, Q. C. Zhang, B. He, R. Pan, Z. X. Wang, M. X. Chen, Z. Wang, K. B. Yin, Y. G. Yao, L. Wei, L. T. Sun, *Adv. Mater.* **2022**, *34*, 2104327.

[10] T. Y. Wu, X. J. Wu, L. H. Li, M. M. Hao, G. Wu, T. Zhang, S. Chen, *Angew. Chem., Int. Ed.* **2020**, *59*, 23800.

[11] Q. C. Zhang, C. W. Li, Q. L. Li, Z. H. Pan, J. Sun, Z. Y. Zhou, B. He, P. Man, L. Y. Xie, L. X. Kang, X. N. Wang, J. Yang, T. Zhang, P. P. Shum, Q. W. Li, Y. G. Yao, L. Wei, *Nano Lett.* **2019**, *19*, 4035.

[12] Y. Zhang, Y. Zhao, X. Cheng, W. Weng, J. Ren, X. Fang, Y. Jiang, P. Chen, Z. Zhang, Y. Wang, H. Peng, *Angew. Chem., Int. Ed.* **2015**, *54*, 11177.

[13] Z. Xu, Y. Liu, X. Zhao, L. Peng, H. Sun, Y. Xu, X. Ren, C. Jin, P. Xu, M. Wang, C. Gao, *Adv. Mater.* **2016**, *28*, 6449.

[14] T. Xu, Z. P. Zhang, L. T. Qu, *Adv. Mater.* **2020**, *32*, 1901979.

[15] W. Ma, Y. Zhang, S. Pan, Y. Cheng, Z. Shao, H. Xiang, G. Chen, L. Zhu, W. Weng, H. Bai, M. Zhu, *Chem. Soc. Rev.* **2021**, *50*, 7009.

[16] F. Mo, G. Liang, Z. Huang, H. Li, D. Wang, C. Zhi, *Adv. Mater.* **2020**, *32*, 1902151.

[17] Q. C. Zhang, P. Man, B. He, C. W. Li, Q. L. Li, Z. H. Pan, Z. X. Wang, J. Yang, Z. Wang, Z. Y. Zhou, X. H. Lu, Z. Q. Niu, Y. G. Yao, L. Wei, *Nano Energy* **2020**, *67*, 104212.

[18] Y. Zeng, Z. Lai, Y. Han, H. Zhang, S. Xie, X. Lu, *Adv. Mater.* **2018**, *30*, 1802396.

[19] H. F. Li, Z. X. Liu, G. J. Liang, Y. Huang, M. S. Zhu, Z. X. Pei, Q. Xue, Z. J. Tang, Y. K. Wang, B. H. Li, C. Y. Zhi, *ACS Nano* **2018**, *12*, 3140.

[20] T. Wu, Z. Ma, Y. He, X. Wu, B. Tang, Z. Yu, G. Wu, S. Chen, N. Bao, *Angew. Chem., Int. Ed.* **2021**, *60*, 10366.

[21] Z. H. Pan, J. Yang, J. Yang, Q. C. Zhang, H. Zhang, Z. K. Kou, Y. F. Zhang, H. Chen, C. L. Yan, J. Wang, *ACS Nano* **2020**, *14*, 842.

[22] X. Xiao, X. Xiao, Y. H. Zhou, X. Zhao, G. R. Chen, Z. X. Liu, Z. H. Wang, C. Y. Lu, M. L. Hu, A. Nashalian, S. Shen, K. D. Xie, W. W. Yang, Y. J. Gong, W. B. Ding, P. Servati, C. Han, S. X. Dou, W. J. Li, J. Chen, *Sci. Adv.* **2021**, *7*, eabl3742.

[23] J. Yan, S. Li, B. Lan, Y. Wu, P. S. Lee, *Adv. Funct. Mater.* **2020**, *30*, 1902564.

[24] H. Qiu, H. Cheng, J. Meng, G. Wu, S. Chen, *Angew. Chem., Int. Ed.* **2020**, *59*, 7934.

[25] Q. C. Zhang, W. W. Xu, J. Sun, Z. H. Pan, J. X. Zhao, X. N. Wang, J. Zhang, P. Man, J. B. Guo, Z. Y. Zhou, B. He, Z. X. Zhang, Q. W. Li, Y. G. Zhang, Y. G. Yao, *Nano Lett.* **2017**, *17*, 7552.

[26] G. X. Qu, J. L. Cheng, X. D. Li, D. M. Yuan, P. N. Chen, X. L. Chen, B. Wang, H. S. Peng, *Adv. Mater.* **2016**, *28*, 3646.

[27] Y. Zhou, C.-H. Wang, W. Lu, L. Dai, *Adv. Mater.* **2020**, *32*, 1902779.

[28] D. Chen, K. Jiang, T. T. Huang, G. Z. Shen, *Adv. Mater.* **2020**, *32*, 1901806.

[29] S. L. Zhai, H. E. Karahan, C. J. Wang, Z. X. Pei, L. Wei, Y. Chen, *Adv. Mater.* **2020**, *32*, 1902387.

[30] M. Liao, C. Wang, Y. Hong, Y. F. Zhang, X. L. Cheng, H. Sun, X. L. Huang, L. Ye, J. X. Wu, X. Shi, X. Y. Kang, X. F. Zhou, J. W. Wang, P. Z. Li, X. M. Sun, P. N. Chen, B. J. Wang, Y. G. Wang, Y. Y. Xia, Y. H. Cheng, H. P. Peng, *Nat. Nanotechnol.* **2022**, *17*, 372.

[31] Z. C. Y. Zhang, B. J. Xi, X. Wang, X. J. Ma, W. H. Chen, J. K. Feng, S. L. Xiong, *Adv. Funct. Mater.* **2021**, *31*, 2103070.

[32] X. Wang, Z. C. Y. Zhang, B. J. Xi, W. H. Chen, Y. X. Jia, J. K. Feng, S. L. Xiong, *ACS Nano* **2021**, *15*, 9244.

[33] X. Wang, B. J. Xi, Z. Y. Feng, W. H. Chen, H. B. Li, Y. X. Jia, J. K. Feng, Y. Y. Qian, S. L. Xiong, *J. Mater. Chem. A* **2019**, *7*, 19130.

[34] R. C. Wei, X. Wang, B. J. Xi, Z. Y. Feng, H. B. Li, W. H. Chen, J. K. Feng, S. L. Xiong, *ACS Appl. Energy Mater.* **2020**, *3*, 5343.

[35] J. Yang, Q. Zhang, Z. Wang, Z. Wang, L. Kang, M. Qi, M. Chen, W. Liu, W. Gong, W. Lu, P. P. Shum, L. Wei, *Adv. Energy Mater.* **2020**, *10*, 2001064.

[36] J. Liu, D. Zhu, T. Ling, A. Vasileff, S.-Z. Qiao, *Nano Energy* **2017**, *40*, 264.

[37] M. H. Yu, X. Y. Cheng, Y. X. Zeng, Z. L. Wang, Y. X. Tong, X. H. Lu, S. H. Yang, *Angew. Chem., Int. Ed.* **2016**, *55*, 6762.

[38] J. Yang, H. Yang, C. Ye, T. Li, G. Chen, Y. Qiu, *Energy Storage Mater.* **2022**, *46*, 472.

[39] C. Guan, W. Zhao, Y. Hu, Q. Ke, X. Li, H. Zhang, J. Wang, *Adv. Energy Mater.* **2016**, *6*, 1601034.

[40] W. Fu, E. Zhao, X. Ren, A. Magasinski, G. Yushin, *Adv. Energy Mater.* **2018**, *8*, 1703454.

[41] M. Yu, Z. Wang, C. Hou, Z. Wang, C. Liang, C. Zhao, Y. Tong, X. Lu, S. Yang, *Adv. Mater.* **2017**, *29*, 1602868.

[42] Y. Zhao, P. Zhang, J. Liang, X. Xia, L. Ren, L. Song, W. Liu, X. Sun, *Energy Storage Mater.* **2022**, *47*, 424.

[43] B. Yao, S. Chandrasekaran, J. Zhang, W. Xiao, F. Qian, C. Zhu, E. B. Duoss, C. M. Spadaccini, M. A. Worsley, Y. Li, *Joule* **2018**, *3*, 459.

[44] Y. Song, T. Liu, B. Yao, M. Li, T. Kou, Z.-H. Huang, D.-Y. Feng, F. Wang, Y. Tong, X.-X. Liu, Y. Li, *ACS Energy Lett.* **2017**, *2*, 1752.

[45] Z.-H. Huang, Y. Song, D.-Y. Feng, Z. Sun, X. Sun, X.-X. Liu, *ACS Nano* **2018**, *12*, 3557.

[46] J. P. liu, C. Guan, C. Zhou, Z. Fan, Q. Q. Ke, G. Z. Zhang, C. Liu, J. Wang, *Adv. Mater.* **2016**, *28*, 8732.

[47] F. Meng, H. Zhong, D. Bao, J. Yan, X. Zhang, *J. Am. Chem. Soc.* **2016**, *138*, 10226.

[48] C. Xia, J. Guo, Y. Lei, H. Liang, C. Zhao, H. N. Alshareef, *Adv. Mater.* **2018**, *30*, 1705580.

[49] F. Wan, Z. Q. Niu, *Angew. Chem., Int. Ed.* **2019**, *58*, 16358.

[50] J. Ding, Z. Du, L. Gu, B. Li, L. Wang, S. Wang, Y. Gong, S. Yang, *Adv. Mater.* **2018**, *30*, 1800762.

[51] X. Dai, F. Wan, L. Zhang, H. Cao, Z. Niu, *Energy Storage Mater.* **2019**, *17*, 143.

[52] M. Occhiuzzi, D. Cordischi, R. Dragone, *J. Solid State Chem.* **2005**, *178*, 1551.

[53] Y. Liu, H. Dai, L. Wu, W. Zhou, L. He, W. Wang, W. Yan, Q. Huang, L. Fu, Y. Wu, *Adv. Energy Mater.* **2019**, *9*, 1901379.

[54] T. Brezesinski, J. Wang, S. H. Tolbert, B. Dunn, *Nat. Mater.* **2010**, *9*, 146.

[55] G. Sun, X. Zhang, R. Lin, J. Yang, H. Zhang, P. Chen, *Angew. Chem., Int. Ed.* **2015**, *127*, 4734.

[56] X. Zheng, L. Yao, Y. Qiu, S. Wang, K. Zhang, *ACS Appl. Energy Mater.* **2019**, *2*, 4335.

[57] C. Zhu, P. Yang, D. Chao, X. Wang, X. Zhang, S. Chen, B. K. Tay, H. Huang, W. Zhang, W. Mai, H. J. Fan, *Adv. Mater.* **2015**, *27*, 4566.

[58] X. Wang, B. Liu, R. Liu, Q. Wang, X. Hou, D. Chen, R. Wang, G. Shen, *Angew. Chem., Int. Ed.* **2014**, *53*, 1849.

[59] Z. Yu, J. Moore, J. Calderon, L. Zhai, J. Thomas, *Small* **2015**, *11*, 5289.

[60] Z. Li, M. Shao, L. Zhou, R. Zhang, C. Zhang, J. Han, M. Wei, D. G. Evans, X. Duan, *Nano Energy* **2016**, *20*, 294.

[61] W. Zuo, C. Xie, P. Xu, Y. Li, J. Liu, *Adv. Mater.* **2017**, *29*, 1703463.

[62] X. Cheng, J. Zhang, J. Ren, N. Liu, P. Chen, Y. Zhang, J. Deng, Y. Wang, H. Peng, *J. Phys. Chem. C* **2016**, *120*, 9685.

[63] P. He, M. Y. Yan, G. B. Zhang, R. M. Sun, L. N. Chen, Q. Y. An, L. Q. Mai, *Adv. Energy Mater.* **2017**, *7*, 1601920.

[64] F. Wan, L. L. Zhang, X. Dai, X. Y. Wang, Z. Q. Niu, J. Chen, *Nat. Commun.* **2018**, *9*, 1656.

[65] D. Yu, K. Goh, H. Wang, L. Wei, W. Jiang, Q. Zhang, L. Dai, Y. Chen, *Nat. Nanotechnol.* **2014**, *9*, 555.